Electronic Supplementary Material

Efficient acetylene/carbon dioxide separation with excellent dynamic capacity and low regeneration energy by anion-pillared hybrid materials

Yijian Li[1], Jianbo Hu[2], Jiyu Cui[1], Qingju Wang[1], Huabin Xing[1,2], Xili Cui (✉)[1,2]

1 Zhejiang Key Laboratory of Smart Biomaterials, Key Laboratory of Biomass Chemical Engineering of Ministry of Education, College of Chemical and Biological Engineering, Zhejiang University, Hangzhou 310027, China
2 ZJU-Hangzhou Global Scientific and Technological Innovation Center, Hangzhou 311215, China

E-mail: cuixl@zju.edu.cn

Experimental Procedures

Materials and methods:

Ammonium hexafluorotitanate ($(NH_4)_2TiF_6$, 99%, Sigma-Aldrich), nickel(II) tetrafluoroborate hexahydrate ($Ni(BF_4)_2•xH_2O$, 99%, J&K Chemical), nickel oxide (NiO, 99.99%, Macklin), niobium pentoxide (Nb_2O_5, 99.99%, Sigma-Aldrich), hydrofluoric acid (HF, 40%, Macklin), 4,4'-dipyridine ($C_{10}H_8N_2$, 98%, Macklin), methanol (CH_3OH, anhydrous, 99%, Sinopharm), ethylene glycol ($C_2H_6O_2$, 99.8%, Sinopharm). All chemicals were obtained from commercial sources and used without further purification.

Powder X-Ray Diffraction (PXRD):

Powder X-ray diffraction (PXRD) data were collected on a SHIMADZU XRD-6000 diffractometer (Cu K_α λ = 1.540598 Å) with an operating power of 40 KV, 30 mA and a scan speed of 4.0°/min. The range of 2θ was from 5° to 60°.

Single crystal X-ray diffraction

Single crystal X-ray diffraction data were collected on a Bruker APEX-II CCD diffractometer equipped with a Mo K_α radiation (λ = 0.71073 Å) at 123 K. In all cases indexing was performed using APEX2 (Difference Vectors method). Data refinement and reduction were performed using Bruker SAINT. Absorption correction was performed by multi-scan method implemented in SADABS. Space group was determined using XPREP implemented in APEX2. Structure was solved using Direct Methods (SHELXS-97) and expanded using Fourier methods and refined on F^2 using full-matrix least-squares techniques with SHELXL-2014.

Thermal Gravimetric Analysis (TGA)

The thermal gravimetric analysis was performed on an instrument of TGA Q500 V20.13 Build 39. Experiments were carried out using a platinum pan under nitrogen atmosphere which conducted by a flow rate of 60 mL/min nitrogen gas or air. Firstly, the sample was removed water at 100 °C and equilibrated for 5 minutes，then cooled down to 50 °C. The data were collected at the temperature range of 50 °C to 650 °C

with a ramp of 5 °C·min^{-1}.

Water stability measurements

Powder sample of ZU-100 were exposed to water at room temperature for several days. After that, each sample was solvent exchanged in methanol and then were evacuated at 65 °C for 12 h until the pressure dropped below 7 μm Hg. The activated samples were characterized by PXRD to detect if the samples had been affected by exposure to humidity.

Calculation of dynamic adsorption capacity and separation factor

The calculation of dynamic adsorption capacity is based on the breakthrough curves which is exhibited in Fig. S2.

$$Q_{pre} = \frac{v}{22.4 \cdot m}(S_1 + S_2) = \frac{v}{22.4 \cdot m \cdot c_0}\int_{0\ pre}^{t_2}(c_0 - c_i)\,\mathrm{dt} \qquad (1)$$

$$Q_L = \frac{v}{22.4 \cdot m}(S_1 - S_3)$$

$$= \frac{v}{22.4 \cdot m \cdot c_0}\{\int_{0\ L}^{t_1}(c_0 - c_i)dt - [\int_{t_1\ L}^{t_2} c_i dt - \int_{t_1\ L}^{t_2} c_0 dt]\} \qquad (2)$$

where Q_{pre} is the equilibrium dynamic adsorption capacity of the preferred gas (mmol g^{-1}), Q_L is the equilibrium dynamic adsorption capacity of the less-preferred gas (mmol g^{-1}). v is the flow rate (mL/min), m is the mass of the column (g). t_1 and t_2 correspond to the special time marked in Fig. S15. c_0 and c_i correspond to the equilibrium concentration and the detected concentration. The separation factor (α) of the breakthrough experiment is determined as:

$$\alpha = \frac{Q_{pre} \cdot y_L}{Q_L \cdot y_{pre}} \qquad (2)$$

where y_i is the molar fraction of gas i (i = L, pre) in the gas mixture.

Calculation of isosteric heat of adsorption (Q_{st})

The binding energy of C_2H_2 or CO_2 is reflected in the isosteric heat of adsorption, Q_{st}, defined as

$$Q_{st} = -\mathrm{R}\sum_{i=0}^{m} a_i N^i \qquad (3)$$

$$\ln P = \ln\mathrm{N} + \frac{1}{T}\sum_{i=0}^{m} a_i N^i + \sum_{j=0}^{n} b_j N^j \qquad (4)$$

A virial-type expression of the above form comprising the temperature-independent parameters a_i and b_j was employed to calculate the enthalpies of adsorption for C_2H_2 and CO_2 at 283 K, 298 K and 313 K on compounds.

Here, P is the pressure described in mmHg, N is the adsorbed amount in mg/g, T is the temperature in K, a_i and b_i are virial coefficients, and m and n represent the number of coefficients used to describe the isotherms. Q_{st} is the coverage-dependent enthalpy of adsorption and R is the universal gas constant.

IAST calculations of adsorption selectivity

In order to predict binary mixture adsorption in ZU-61 and ZU-100, the dual-site Langmuir-Freundlich (DSLF) equation is used for fitting the single-component C_2H_2 and CO_2 adsorption isotherm data.

$$q = q_{A,sat}\frac{b_A p^{1/n_A}}{1 + b_A p^{1/n_A}} + q_{B,sat}\frac{b_B p^{1/n_B}}{1 + b_B p^{1/n_B}} \qquad (3)$$

where q is the amount adsorbed per mass of adsorbent (mol·kg^{-1}), p is the pressure of the bulk gas at equilibrium with the adsorbed phase (kPa), $q_{A,sat}$ and $q_{B,sat}$ are the saturation loadings of sites A and B (mol·kg^{-1}), b_A and b_B are the affinity coefficients to the sites A and B (1/kPa), n_A and n_B represent the deviations from an ideal homogeneous surface. The adsorption selectivity of component i over component j was defined by the following equation:

$$S_{ij} = \frac{q_i/q_j}{p_i/p_j} \qquad (4)$$

where q_i and q_j represent the equilibrated adsorption molar loading of component i and j respectively, p_i and p_j represent the partial pressure of component i and j in bulk gas phase respectively.

Dispersion-corrected density-functional theory calculations

Dispersion-corrected density-functional theory (DFT-D) calculations were performed using the Quantum-Espresso package. A semi-empirical addition of dispersive forces to conventional DFT-D was included in the calculation to account for van der Waals interactions [1]. We used Vanderbilt-type ultrasoft pseudopotentials and generalized gradient approximation (GGA) with Perdew-Burke-Ernzerhof (PBE) exchange correlation [2]. A cutoff energy of 544 Ev and a 2×2×3 k-point mesh (generated using the Monkhosrt-Pack scheme) were found to be enough for the total energy to converge within 0.01 meV·atom^{-1}. We first optimized the structure of ZU-100 and ZU-61. The optimized structures are good matches for the experimentally determined crystal structures of the coordination networks. Various guest gas molecules were then introduced to various locations of the channel pore, followed by a full structural relaxation. To obtain the gas binding energy, an isolated gas molecule placed in a supercell (with the same cell dimensions as the MOF crystal) was also relaxed as a reference. The static binding energy (at T = 0 K) was then calculated using: EB = E(MOF) + E(gas) – E(MOF+gas).

Tables and Figures

Table S1. Crystal structure data for ZU-100 and ZU-61.

Unit cell parameters		
Materials	ZU-100	ZU-61 [23]
Formula sum	C20 H16 F6 N4 Ni Ti	C20 H18 F5 N4 Nb Ni O2
Formula weight	533	593
Crystal system	tetragonal	tetragonal
Space-group	P 4/mmm	P 4/mmm

Unit cell dimensions	a=b=11.2557(2) Å, c=7.9309(2) Å	a=b=11.2649 Å, c=7.8859 Å
Cell ratio	a/b=1.0000 b/c=1.4192 c/a=0.7046	a/b=1.0000 b/c=1.4285 c/a=0.7000
Cell volume	1004.77(6) $Å^3$	1000.70 $Å^3$
Z	1	1

Table S2. The DFT-D calculated results of C_2H_2 and CO_2 in ZU-61 and ZU-100

	ZU-61		ZU-100	
	C_2H_2	CO_2	C_2H_2	CO_2
Distance of C-H⋯F or C⋯F bond (Å)	2.014	2.753	1.950	2.696
Binding energy (kJ/mol)	44.6	29.8	46.9	28.7

Table S3. The storage density of C_2H_2 in the pore of various MOF materials at 1 bar.

Materials	C_2H_2 static uptake at 298K and 1bar ($cm^3 \cdot g^{-1}$)	Uptake ratio at 1bar and 298K (C_2H_2/CO_2)	C_2H_2 dynamic uptake ($cm^3 \cdot g^{-1}$)	Ref.
HKUST-1	201	1.78	-	[3]
MFM-188	232.6	1.93	-	[4]
MAF-2	70	3.68	-	[5]
Mg-MOF-74	184.4	1.03	-	[6]
UTSA-74-Zn	145	1.61	-	[7]
JCM-1	76.5	2.01	49.3	[8]
PCP-33	121.8	2.08	-	[9]
SIFSIX-3-Ni	81.5	1.43	-	[10]
SIFSIX-2-Cu-i	90	0.83	-	[10]
UTSA-300a	68.9	21.2	-	[11]
NKMOF-1-Ni	61	1.19	-	[12]
DICRO-4-Ni-i	41	1.82	-	[13]
HOF-3	47	2.24	25.5	[14]
FJU-22a	114.8	1.03	44.1	[15]
FJU-90	180	1.74	41.9	[16]
$Ni_3[HCOO]_6$	90	1.43	37.4	[17]
ZU-61	143	2.28	46.3	This work
ZU-100	186	1.89	105.4	This work
JXNU-5	55.9	1.61	16.3	[18]
ATC-Cu	112.2	1.25	-	[19]
BSF-3	80.4	1.70	65.0	[20]
SIFSIX-Cu-TPA	185	1.73	140	[21]
SNNU-45	134	1.38	127	[22]

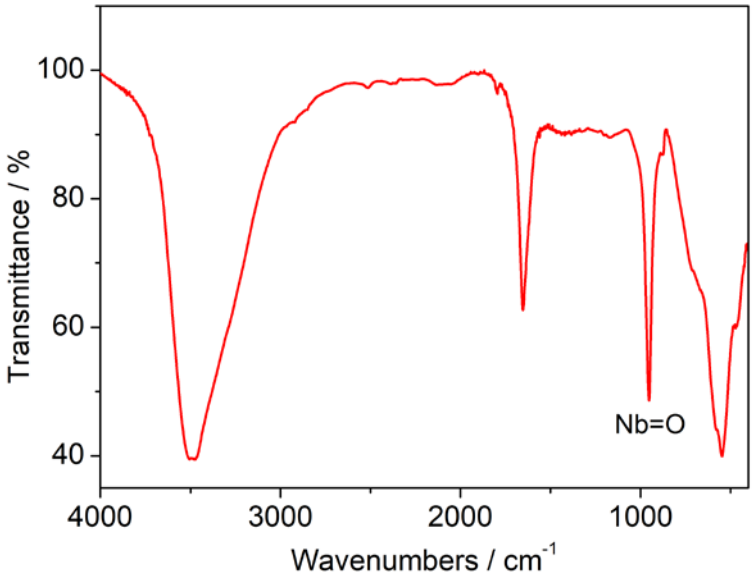

Fig. S1. IR spectrum of $NiNbOF_5$

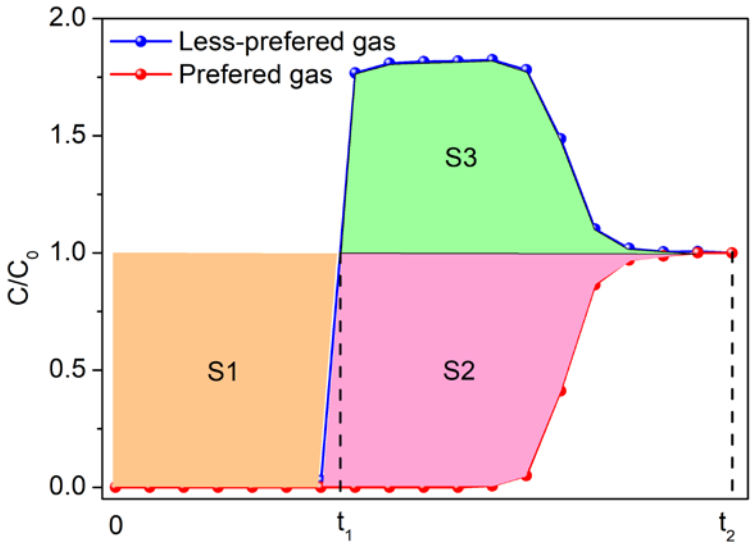

Fig. S2. Schematic of dynamic capacity calculation.

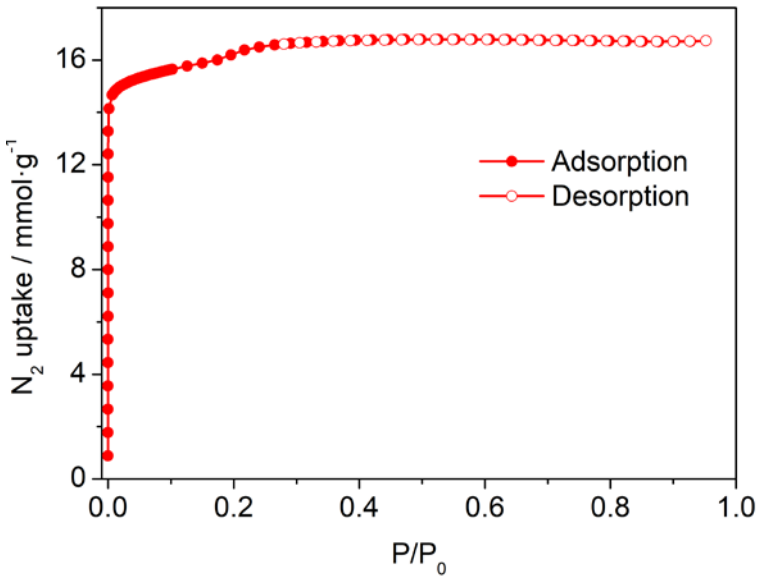

Fig. S3. N_2 adsorption-desorption isotherms of ZU-100 at 77 K

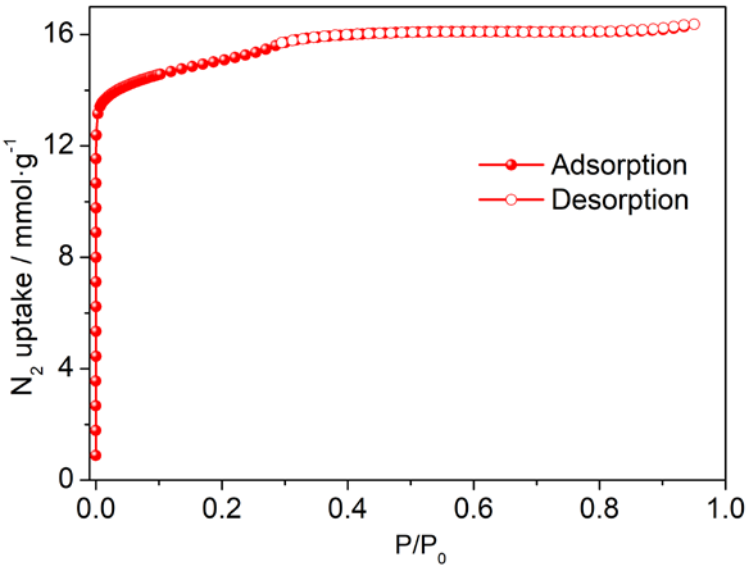

Fig. S4. N_2 adsorption-desorption isotherms of ZU-61 at 77 K

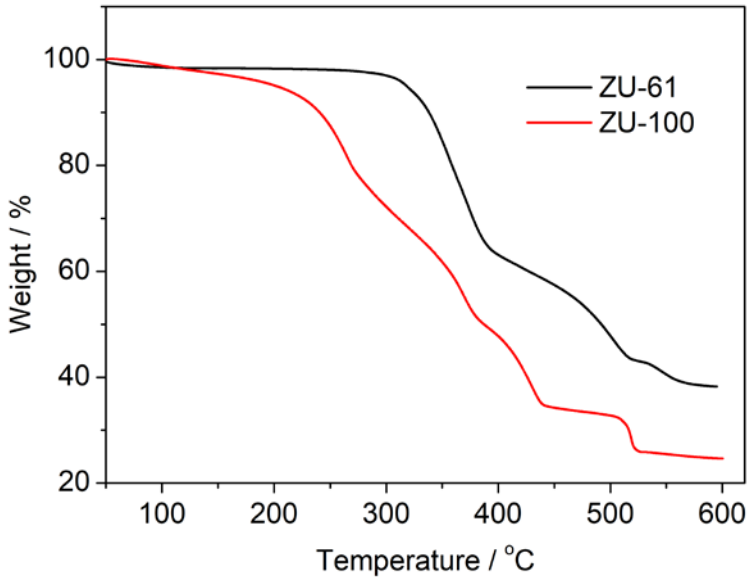

Fig. S5. Comparison of thermogravimetric curves of ZU-61 and ZU-100.

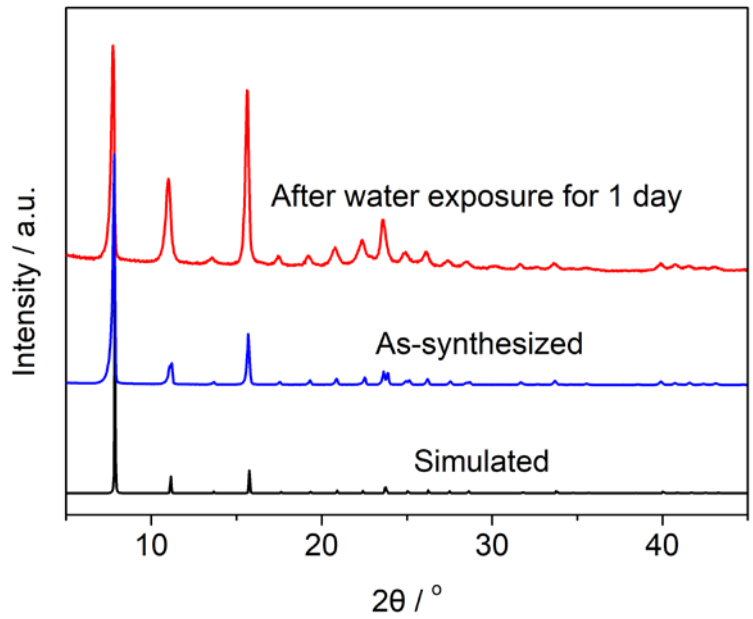

Fig. S6. PXRD patterns of synthesized powder (blue), powder exposed in water for 1 day (red) and the calculated PXRD pattern (black) of ZU-100.

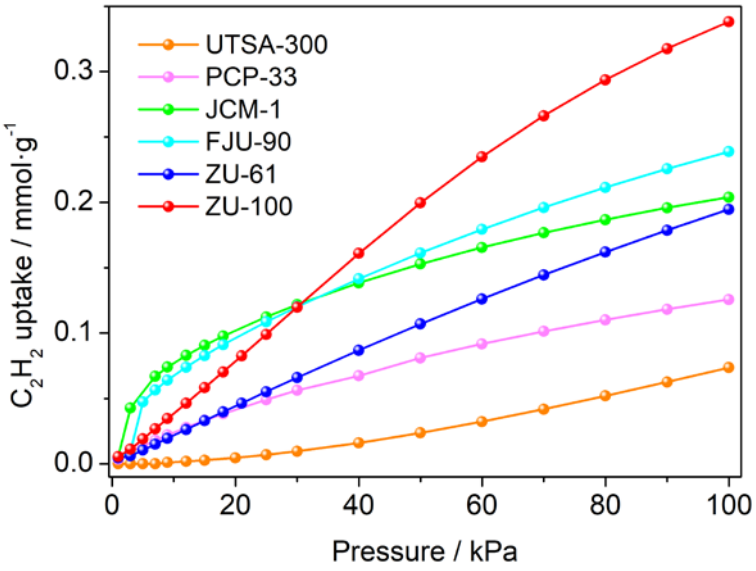

Fig. S7. Calculated C_2H_2 adsorption isotherms from C_2H_2/CO_2 (1/99, v/v) mixtures at 298 K.

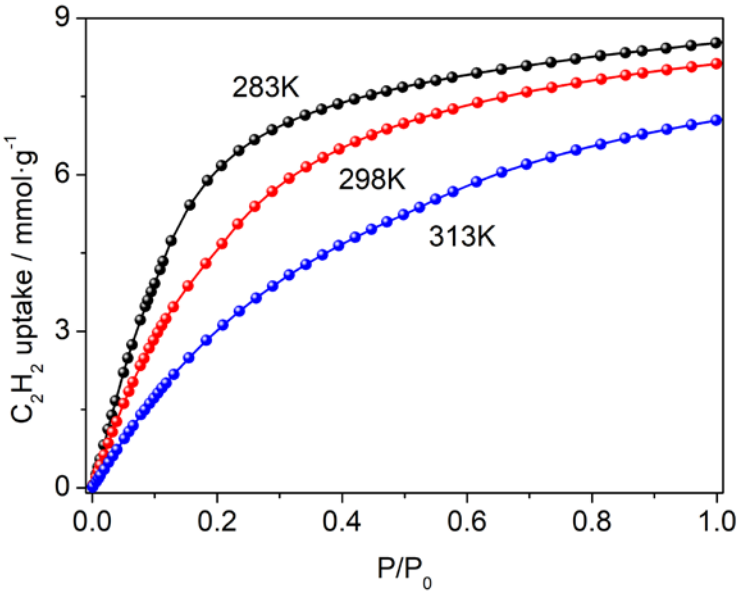

Fig. S8. Static adsorption isotherms of C_2H_2 on ZU-100 at 283, 298 and 313 K.

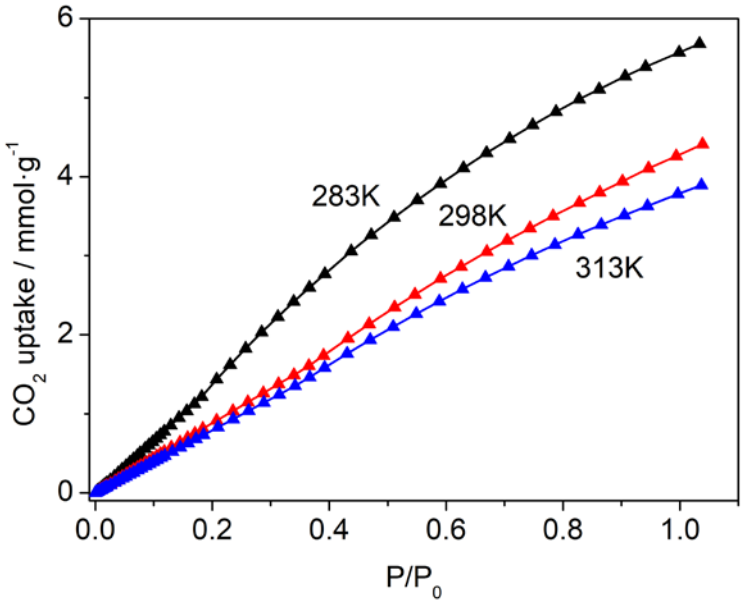

Fig. S9. Static adsorption isotherms of CO_2 on ZU-100 at 283, 298 and 313 K.

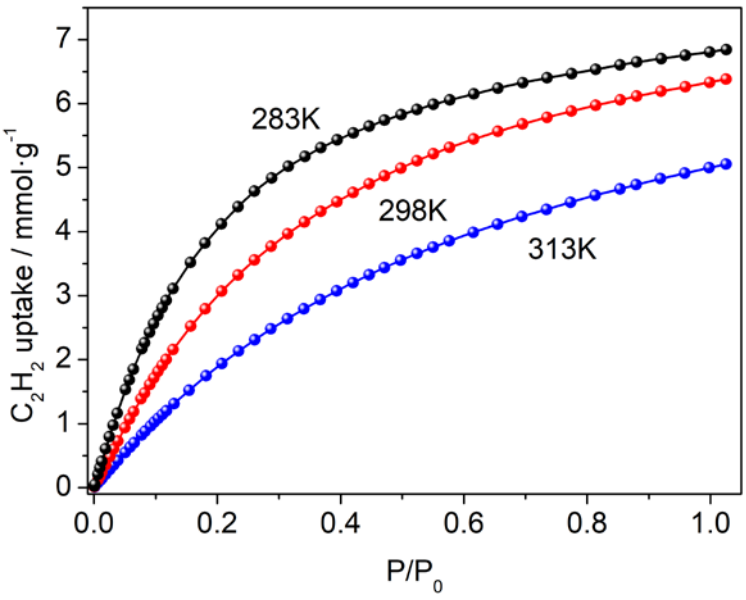

Fig. S10. Static adsorption isotherms of C_2H_2 on ZU-61 at 283, 298 and 313 K.

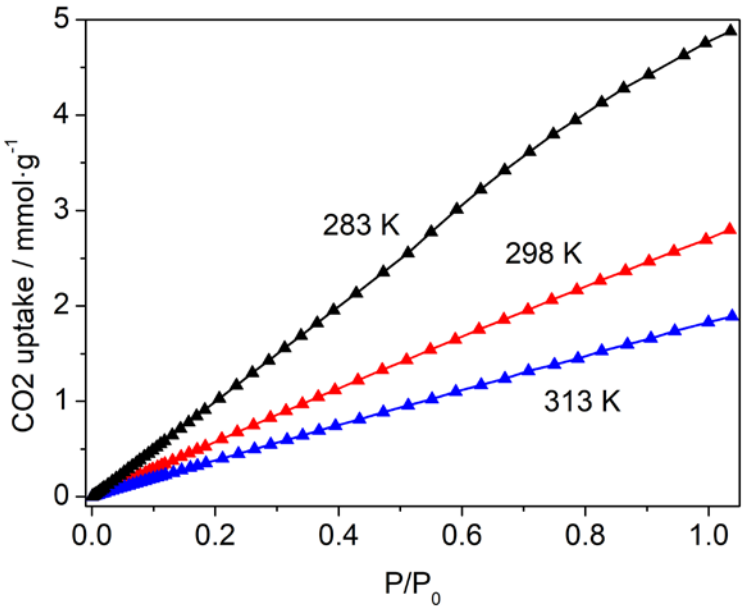

Fig. S11. Static adsorption isotherms of CO_2 on ZU-61 at 283, 298 and 313 K.

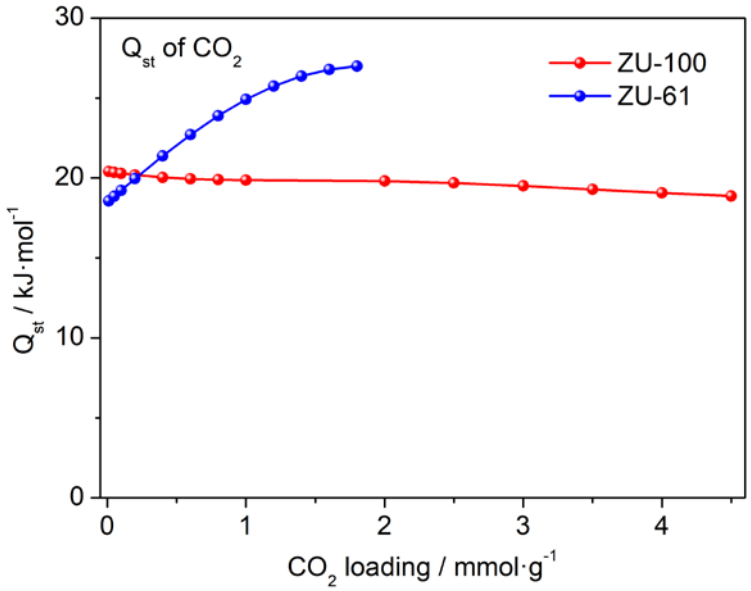

Fig. S12. Calculated isosteric heats of adsorption for CO_2 at different CO_2 loadings on ZU-61 and ZU-100.

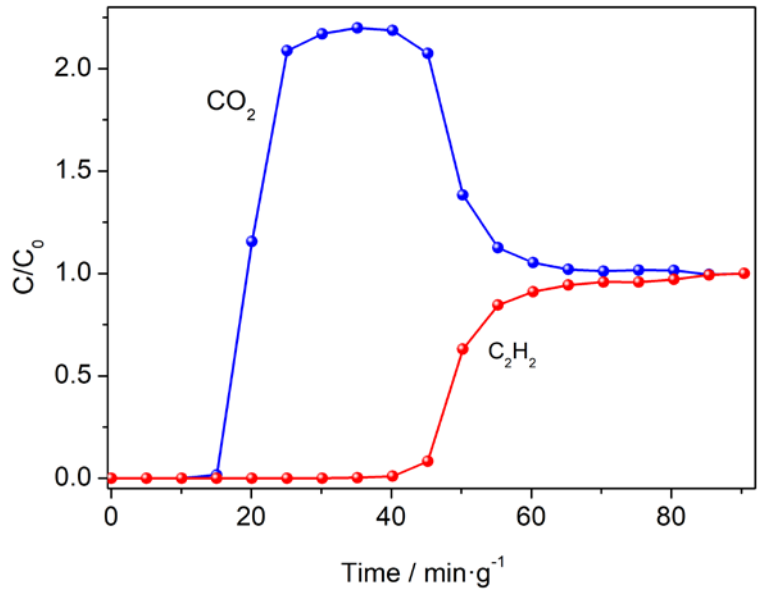

Fig. S13. Experimental dynamic breakthrough curves for C_2H_2/CO_2 (50/50, v/v) separations with ZU-100 at 298 K and 1 bar. (mixed gas flow: 4 ml·min^{-1})

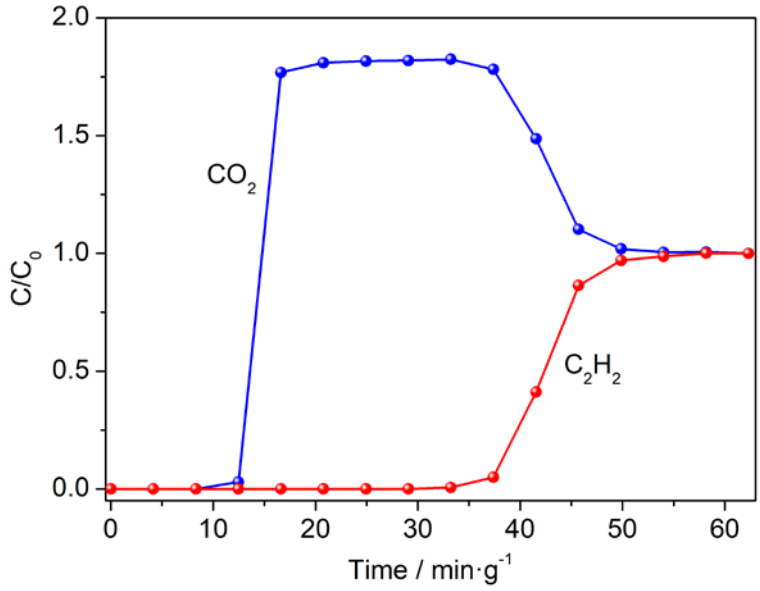

Fig. S14. Experimental dynamic breakthrough curves for C_2H_2/CO_2 (50/50, v/v) separations with ZU-61 at 298 K and 1 bar. (mixed gas flow: 4 ml·min^{-1})

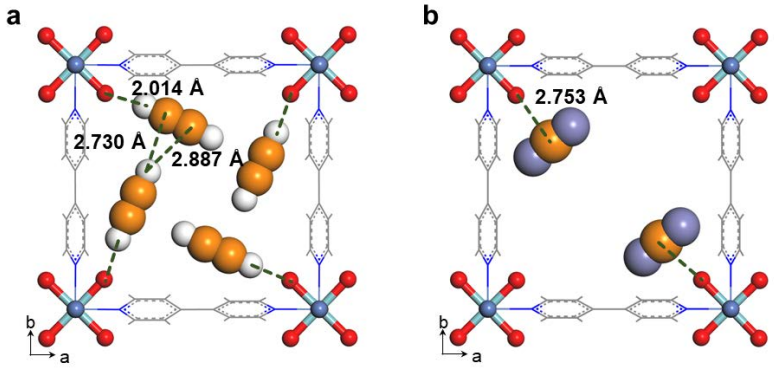

Fig. S15. Schematic pictures showing the DFT optimized (a) C_2H_2 and (b) CO_2 adsorption configurations and the distances between atoms (Å) in ZU-61. (Color code: F red; Ni, O purple; Nb cyan; N blue; C orange; H white).

References

1. Barone V, Casarin M, Forrer D, Pavone M, Sambi M, Vittadini A. Role and effective treatment of dispersive forces in materials: polyethylene and graphite crystals as test cases. Journal of Computational Chemistry, 2009, 30(6): 934–939
2. Myers A L, Prausnitz J M. Thermodynamics of mixed-gas adsorption. AIChE Journal, 1965, 11(1): 121–127
3. Xiang S, Zhou W, Gallegos J M, Liu Y, Chen B L. Exceptionally high acetylene uptake in a microporous metal-organic framework with open metal sites. Journal of the American Chemical Society, 2009, 131(34): 12415-9
4. Moreau F, da Silva I, Al Smail N, Easun T, Savage M, Godfrey M, Parker S, Manuel P, Yang S, Schroder M. Unravelling exceptional acetylene and carbon dioxide adsorption within a tetra-amide functionalized metal-organic framework. Nature Communications, 2017, 8: 14085
5. Zhang J, Chen X. Optimized acetylene/carbon dioxide sorption in a dynamic porous crystal. Journal of the American Chemical Society, 2009, 131(15): 5516-5521
6. Caskey S, Wong-Foy A, Matzger A. Dramatic tuning of carbon dioxide uptake via metal substitution in a coordination polymer with cylindrical pores. Journal of the American Chemical Society, 2008, 130(33): 10870-10871
7. Luo F, Yan C, Dang L, Krishna R, Zhou W, Wu H, Dong X, Han Y, Hu T L, O'Keeffe M, et al. UTSA-74: a MOF-74 isomer with two accessible binding sites per metal center for highly selective gas separation. Journal of the American Chemical Society, 2016, 138(17): 5678-5684
8. Lee J, Chuah C Y, Kim J, Kim Y, Ko N, Seo Y, Kim K, Bae T H, Lee E. Separation of acetylene from carbon dioxide and ethylene by a water-stable microporous metal-organic framework with aligned imidazolium groups inside the channels. Angewandte Chemie International Edition, 2018, 57(26): 7869-7873
9. Duan J, Jin W, Krishna R. Natural gas purification using a porous coordination polymer with water and chemical stability. Inorganic Chemistry, 2015, 54(9): 4279-4284
10. Chen K J, Scott H, Madden D, Pham T, Kumar A, Bajpai A, Lusi M, Forrest K, Space B, Perry J, et al. Benchmark C_2H_2/CO_2 and CO_2/C_2H_2 separation by two closely related hybrid ultramicroporous materials. Chem., 2016, 1(5): 753-765
11. Lin R B, Li L, Wu H, Arman H, Li B, Lin R G, Zhou W, Chen B. Optimized separation of acetylene from carbon dioxide and ethylene in a microporous material. Journal of the American Chemical Society, 2017, 139(23): 8022-8028
12. Peng Y, Pham T, Li P, Wang T, Chen Y, Chen K J, Forrest K A, Space B, Cheng P, Zaworotko M J, et al. Robust ultramicroporous metal-organic frameworks with benchmark affinity for acetylene. Angewandte Chemie International Edition,

2018, 57(34): 10971-10975
13. Scott H S, Shivanna M, Bajpai A, Madden D G, Chen K J, Pham T, Forrest K A, Hogan A, Space B, Perry J J, et al. Highly selective separation of C_2H_2 from CO_2 by a new dichromate-based hybrid ultramicroporous material. ACS Applied Materials Interfaces, 2017, 9(39): 33395-33400
14. Li P, He Y, Zhao Y, Weng L, Wang H, Krishna R, Wu H, Zhou W, O'Keeffe M, Han Y, et al. A rod-packing microporous hydrogen-bonded organic framework for highly selective separation of C_2H_2/CO_2 at room temperature. Angewandte Chemie International Edition, 2015, 54(2): 574-577
15. Yao Z, Zhang Z, Liu L, Li Z, Zhou W, Zhao Y, Han Y, Chen B, Krishna R, Xiang S. Extraordinary separation of acetylene-containing mixtures with microporous metal-organic frameworks with open O donor sites and tunable robustness through control of the helical chain secondary building units. Chemistry-A European Journal, 2016, 22(16): 5676-83
16. Ye Y, Ma Z, Lin R B, Krishna R, Zhou W, Lin Q, Zhang Z, Xiang S, Chen B. Pore space partition within a metal-organic framework for highly efficient C_2H_2/CO_2 separation. Journal of the American Chemical Society, 2019, 141(9): 4130-4136
17. Zhang L, Jiang K, Zhang J, Pei J, Shao K, Cui Y, Yang Y, Li B, Chen B, Qian G. Low-cost and high-performance microporous metal–organic framework for separation of acetylene from carbon dioxide. ACS Sustainable Chemistry & Engineering, 2019, 7(1) 1667-1672
18. Liu R, Liu Q, Krishna R, Wang W, He C, Wang Y. Water-stable europium 1,3,6,8-tetrakis(4-carboxylphenyl)pyrene framework for efficient C_2H_2/CO_2 separation. Inorganic Chemistry, 2019, 58(8): 5089-5095
19. Niu Z, Cui X, Pham T, Verma Gaurav, Lan P, Shan C, Xing H, Forrest K, Suepaul S, Space B, et al. A MOF-based ultra-strong acetylene nano-trap for highly efficient C_2H_2/CO_2 separation. Angewandte Chemie International Edition, 2021, 60(10): 5283-5288
20. Zhang Y, Hu J, Krishna R, Wang L, Yang L, Cui X, Duttwyler S, Xing H. Rational design of microporous MOFs with anionic boron cluster functionality and cooperative dihydrogen binding sites for highly selective capture of acetylene. Angewandte Chemie International Edition, 2020, 59(40): 17664-17669
21. Li H, Liu C, Chen C, Di Z, Yuan D, Pang J, Wei W, Wu M, Hong M. An unprecedented pillar-cage fluorinated hybrid porous framework with highly efficient acetylene storage and separation. Angewandte Chemie International Edition, 2021, 60(14): 7547-7552
22. Li Y, Wang Y, Xue Y, Li H, Zhai Q, Li S, Jiang Y, Hu M, Bu X. Ultramicroporous building units as a path to bi-microporous metal-organic frameworks with high acetylene storage and separation performance. Angewandte Chemie International Edition, 2019, 58(38): 13590-13595
23. Cui X, Niu Z, Shan C, Yang L, Hu J, Wang Q, Lan P C, Li Y, Wojtas L, Ma S, et al. Efficient separation of xylene isomers by a guest-responsive metal-organic framework with rotational anionic sites. Nature Communications, 2020, 11: 5456